Available online at www.sciencedirect.com
ScienceDirect
Thermochimica Acta 451 (2006) 34–43
thermochimica acta
www.elsevier.com/locate/tca

Exothermic reactions in Al–CuO nanocomposites

Swati M. Umbrajkar, Mirko Schoenitz, Edward L. Dreizin *

New Jersey Institute of Technology, Newark, NJ 07102, USA

Received 28 June 2006; received in revised form 1 September 2006; accepted 7 September 2006
Available online 16 September 2006

Abstract

Heterogeneous reactions in the Al–CuO system were investigated using differential scanning calorimetry combined with structural and phase analyses of partially reacted samples. The dense nanocomposite 2Al + 3CuO powders used in this study were prepared by arrested reactive milling. Ignition experiments with the powders heated at different rates were also performed and compared to the results of thermal analysis. The results of thermal analysis measurements were processed using isoconversion techniques and a multistep reaction mechanism was proposed to describe the experiments. The reaction between Al and CuO started at ∼400 K and was well described by four parallel reaction steps. The kinetic descriptions of individual steps depend on the frequency factors specific for the powders used in this study and activation energies that should remain valid for any Al–CuO composite materials. The values of the frequency factors and activation energies were determined as well as the specific reaction mechanisms describing each reaction step. The identified reaction steps were tentatively assigned to specific processes of CuO decomposition followed by diffusion of reacting species through amorphous and then crystalline Al_2O_3 polymorphs. Ignition of the nanocomposite Al–CuO materials was shown to be driven primarily by the lower-temperature oxidation processes. It was shown that ignition of Al–CuO nanocomposite powders can be described reasonably well using the proposed kinetics of Al–CuO heterogeneous reactions.

Keywords: Kinetic parameters; Thermites; Nanocomposites; Modeling; Ignition

1. Introduction

Unique nanostructured materials, including reactive nanocomposite powders based on exothermic thermite reactions, have attracted a great deal of interest. Different types of reactive nanocomposites have been synthesized, such as mixed nanopowders (also called metastable intermolecular composites, or MIC) [1–3], porous nanocomposites produced by sol–gel synthesis [4,5], multilayer nanofoils [6,7], and dense nanocomposite powders produced by arrested reactive milling (ARM) [8–10]. Despite different synthesis techniques and material types, the common approach has been to increase the interface area available for heterogeneous reaction between solid fuel and oxidizer components. The ARM technique used in this work to prepare nanocomposite powders is derived from mechanical milling of starting components capable of highly exothermic reaction [11]. For such components, the reaction can be mechanically triggered during the milling and become self-sustained [12]. In ARM, the milling is stopped just before the reaction is initiated [8]. The products are micron-sized powders, which contain reactive components mixed on a nanoscale. The nanocomposites are nearly 100% dense, and their external surface is relatively small, unlike that of the nanocomposites produced from mixed nanopowders. Therefore, only a small fraction of metal oxidizes upon exposure to air producing a thin external passivating oxide layer while bulk of the metal remains reactive. ARM synthesis is a “top-down” process, that is, the synthesis of nanocomposites by continuous refinement of micron-scale starting materials and is readily scalable. Thus, the ARM nanocomposites can be less expensive than similar compositions produced using alternative, “bottom-up” approaches, where nanoparticles or composites are grown from molecular precursors [1–5].

Among several types of reactive nanocomposites synthesized by ARM [8–10], Al–CuO thermites are of particular interest. The reaction is highly exothermic and its temperature can be adjusted to produce either molten or vapor-phase copper. Thus, a broad range of potential applications is possible including joining compounds and energetic compositions enabling transient gas generation. Recently, Al–CuO_x multilayer nanofoils were produced and characterized [6,7]. Differential thermal analysis

* Corresponding author. Tel.: +1 973 596 3327; fax: +1 973 642 4282.
E-mail address: dreizin@njit.edu (E.L. Dreizin).

0040-6031/$ – see front matter © 2006 Elsevier B.V. All rights reserved.
doi:10.1016/j.tca.2006.09.002

traces of these nanofoils when heated from ambient conditions to 1673 K indicated that the reaction proceeded via two separate exotherms occurring around 850–950 and 975–1275 K. These events were interpreted as reactions controlled by lateral growth of Al_2O_3 nuclei and then by diffusion of oxygen through growing Al_2O_3 layers, respectively. It was suggested that the oxygen diffusion through CuO_x layers was not a rate-limiting process for the observed reactions [7]. However, in our initial experiments with Al–CuO dense nanocomposite powders produced by ARM, exothermic events were observed to occur at much lower temperatures, staring from about 400 K [13]. Thus, the reaction mechanisms proposed in refs. [6,7] need to be expanded and verified in order to be applied to a broader range of Al–CuO nanocomposites. The present study is aimed to develop a more adequate description of Al–CuO thermite reactions. Furthermore, the correlation of different processes occurring during such reactions and ignition of Al–CuO nanocomposites occurring at high heating rates was of interest. Differential scanning calorimetry (DSC), X-ray diffraction (XRD) and heated filament ignition experiments [14] were used to quantify the ignition kinetics and related reaction mechanisms.

2. Experimental

2.1. Preparation of nanocomposite powders

A shaker mill (8000 series by Spex CertiPrep) was employed in this research. Flat-ended steel vials were used along with 5 mm steel balls. Starting blends were prepared in stoichiometric proportions from powders of elemental aluminum (99% pure, −325 mesh by Atlantic Equipment Engineers) and cupric oxide CuO (99% pure, 1–5 μm, by Atlantic Equipment Engineers). Synthesis was carried out in argon environment. A small amount of hexane (C_6H_{14}) was added as a process control agent (PCA) to hinder the cold welding during milling. The process temperature was monitored using thermistors attached to the sides of the milling vials and connected to a digital data logger. The instant of reaction was marked by a sharp rise in the vial temperature.

Table 1
Nanocomposite powder samples prepared and used in this research (batch mass 3 g; ball to powder mass ratio 5; 5 mm steel balls)

Sample ID	Hexane (ml)	Milling time (min)
1	0	2
2	1	16
3	8	60

Highly metastable energetic nano-composites were prepared by arresting the milling before the spontaneous exothermic reaction. When the amount of PCA added to the mixture was varied, the milling times required to initiate the reaction changed. Three different samples were prepared by varying both the amount of PCA and the milling times, as shown in Table 1. When the materials were milled without any PCA, the reaction occurred within 2 min. When 1 ml of hexane was added, the reaction was triggered after 16 min of milling. When 8 ml of hexane was added, the reaction did not initiate even after an hour of milling and the metastable samples were prepared by stopping milling after 60 min. For each sample, several 3 g batches were prepared using a ball to powder mass ratio of 5.

2.2. Sample characterization

Morphology and composition of the composites were examined on a LEO 1530 field emission scanning electron microscope (SEM) operated at 10 kV. The samples were embedded in epoxy and cross-sectioned for examination. The phase composition was determined for each sample by X-ray diffraction (XRD). The XRD was performed on a Phillips X'pert MRD powder diffractometer operated at 45 kV and 40 mA using Cu Kα radiation (λ = 1.5438 Å). Temperature-dependent structural transformations were determined by differential scanning calorimetry (DSC) using a Netzsch Simultaneous Thermal Analyzer STA409 PC. Alumina pans were used and the furnace was flushed with argon at approximately 10 ml/min. DSC traces were recorded between room temperature and 1013 K with heating

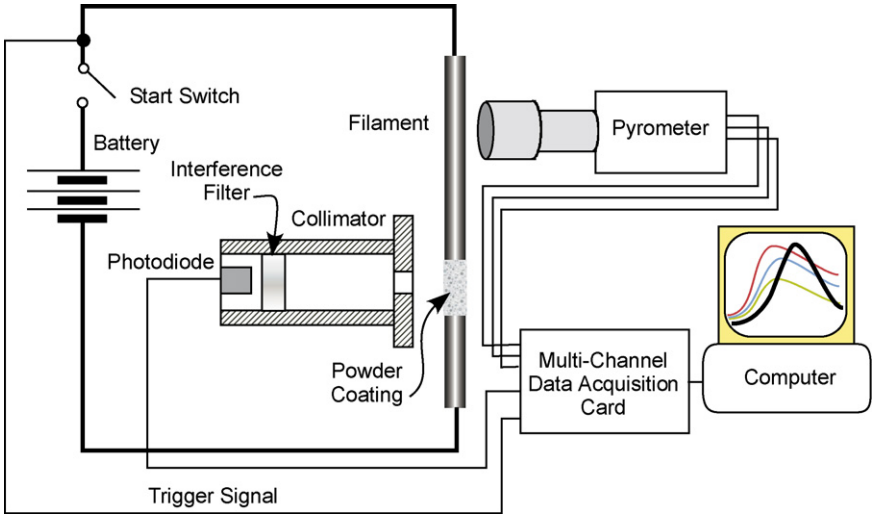

Fig. 1. Heated filament setup used for powder ignition experiments.

rates varying from 5 to 40 K/min. The temperature is accurate within ±1 K.

2.3. Ignition experiments

The powders were ignited in air on the surface of an electrically heated metal filament. Experimental details have been described elsewhere [14,15], but are briefly summarized here for completeness. A simplified diagram of the experimental set-up is shown in Fig. 1. A 0.5 mm diameter Nichrome® wire mounted in a controlled environment chamber was used as a filament. The total length of the heated filament was 4.5 cm; however, the length of the powder coated portion was approximately 1 cm. A small amount of powder was mixed with hexane and a thin layer of the slurry was deposited on the filament surface using a soft paintbrush. The coating was completely dried before the filament was electrically heated. To observe ignition, a silicon photodiode (DET110 by Thorlabs, Inc.) equipped with an iris was aimed at the powder coating at a distance of 4–5 cm. The temperature history of the heated filament was measured using a high-speed infrared pyrometer (DP1581 by Omega Engineering, Inc.). The pyrometer acquired data at a rate of 1000 data points per second. The pyrometer was focused on the uncoated surface of the filament adjacent to the powder coating. Thus, the temperature of the heated powder was not measured directly, but inferred from the measured filament temperature [16]. The filament emissivity was set to $\varepsilon = 0.75$ at the pyrometer controller unit; this is the average emissivity for nichrome in the temperature range of 770–1270 K [17]. A new filament was used for each individual run. The filament heating rate was controlled by varying the dc voltage and using a set of resistors to adjust the current. The heating rates used in these experiments were on the order of 10^3–10^4 K/s. The specific heating rates achieved in individual runs were determined from the recorded filament temperature histories. Both the photodiode and pyrometer outputs were recorded using a PCI-MIO-16E-4 DAQ board by National Instruments, and a LabView-based digital oscilloscope.

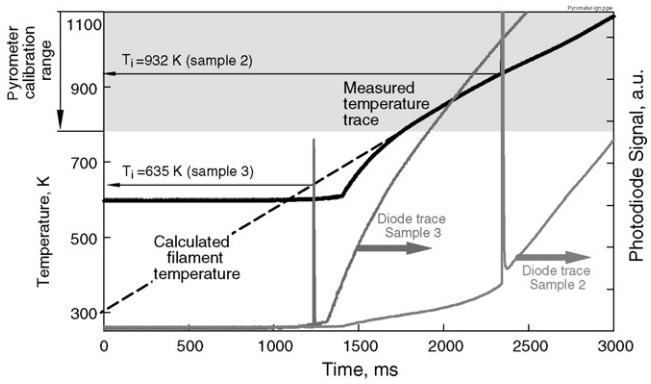

Fig. 2. Photodiode and temperature traces recorded during heated filament ignition experiments of the Al–CuO nanocomposite powders.

Fig. 2 illustrates the ignition temperature measurements and shows a temperature trace corresponding to a specific setting of the electric circuit and two photodiode signatures recorded at this setting for two different powder samples undergoing ignition. The shaded portion of the plot shows the range of temperatures for which the pyrometer was calibrated. For the diode trace labeled as sample 2 (cf. Table 1), the ignition resulting in a sharp spike in the photodiode signal is observed at about

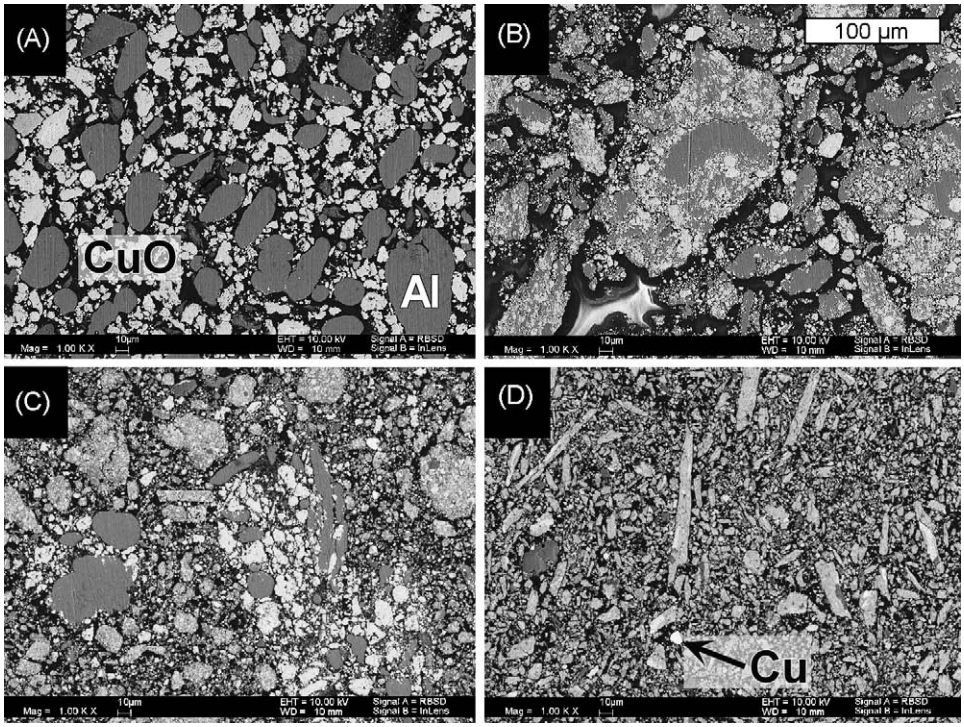

Fig. 3. Backscattered electron SEM images of the cross-sectioned Al–CuO samples embedded in epoxy: (A) starting material; (B) sample 1; (C) sample 2; (D) sample 3. The magnification is the same for all the images and is illustrated by the scale bar in the image B.

2350 ms. At that time, the pyrometer output is within the calibrated temperature range and thus, the ignition temperature is measured directly. Such direct measurements of ignition temperatures were possible for both samples 1 and 2. However for the sample 3 (see the respective trace in Fig. 2) the ignition was observed at a lower temperature. In Fig. 2, the ignition peak occurs at about 1250 ms and the temperature is too low to measure directly from the pyrometer trace. Therefore, for such experiments the ignition temperature was evaluated using a numerical transient model of the filament heating [15]. The model considered the temperature-dependent resistance of the filament, convective heat losses, electric voltage applied, and constant temperature boundary conditions for the filament ends clamped to the massive electrodes. The predicted temperature history of the filament essentially coincided with the experimental data for the range where the temperature measurements were calibrated. Thus, the calculated temperatures corresponding to the lower-temperature portion of the filament heating history could be used to evaluate the ignition temperature as illustrated in Fig. 2.

3. Results

3.1. SEM analysis

Fig. 3 shows SEM images of the cross-sections of the starting powder mixture and Al–CuO composites synthesized after ~2, 16 and 60 min of milling. These images are produced using backscattered electrons and show phase contrast between Al and CuO-rich phases. It can be observed that the particle size decreases and morphology of the powder changes with increasing milling times. For the starting mixture, (Fig. 3A) the bright CuO particles are well distinguished from gray Al and the dark epoxy background. After 2 min of dry milling (sample 1), the Al particles are flattened as shown in Fig. 3B. The CuO particles are reduced in size and embedded in aluminum. Very large, dense agglomerates are formed. Most of the CuO particles are close to the surface of aluminum and located on or between the ductile aluminum layers. After 16 min of milling with 1 ml of hexane added (Fig. 3C, sample 2), the particle sizes of Al and CuO reduce drastically and some of the CuO particles become embedded in the Al matrix. However, unmixed particles of Al and CuO are still present. The particle sizes vary widely. The mixing appears to be non-homogeneous throughout the sample. Groups of relatively coarse particles of Al and CuO representing loose agglomerates are visible in Fig. 3C. At the same time, some particles with a much finer mixing of components are also present. Fig. 3D shows that the increase in the milling time to 60 min, possible when 8 ml of hexane was added, resulted in further reduction of the particle sizes and in a more homogeneous mixing. Fig. 4 shows an image of the same sample as shown in Fig. 3D but at a higher magnification. Most of the particles are nanocomposites of CuO inclusions in the aluminum matrix. Fine mixing of Al and CuO particles has been achieved. At the same time, several very bright and homogeneous particles are visible. A close inspection shows presence of small spherical voids inside such bright particles, which are identified as copper. Therefore, at the extended milling time and large amounts of the PCA used, the thermite reaction occurred locally, but did not propagate through the entire sample. This suggestion is further confirmed by XRD as described below.

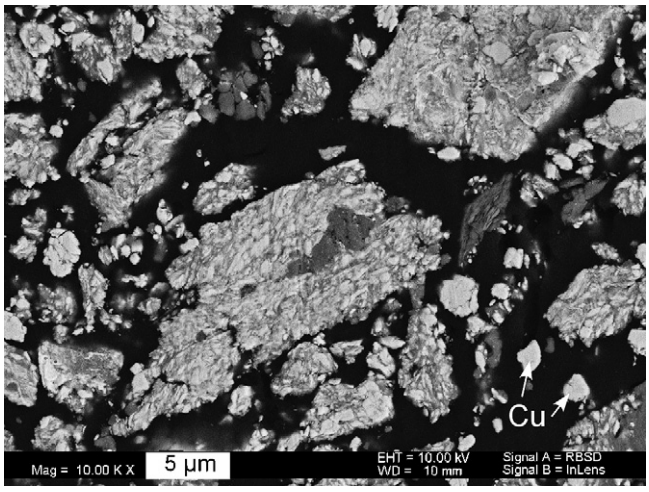

Fig. 4. High magnification SEM image of cross-sectioned sample 3 embedded in epoxy.

3.2. X-ray analysis

Fig. 5 shows the X-ray diffraction patterns for the samples 1–3. As seen earlier in Table 1, addition of hexane enables increased milling time. As an overall trend, the increased milling times result in the decreased intensity of Al and CuO peaks. The XRD pattern of sample 1 shows only peaks of starting materials, Al and CuO. The XRD pattern of sample 2 indicates additional presence of Cu and small amounts of Cu_2O. These peaks arise due to the localized partial reaction that occurs during milling. Amorphous or poorly crystalline Al_2O_3 polymorphs are also likely to be produced in this reaction, but are not detected from XRD. Extended milling time (60 min) for sample 3 gives rise to $CuAl_2$, γ-alumina and Cu_9Al_4 in addition to Al, CuO, Cu and Cu_2O peaks. Increase in the milling time also leads to broadening of peaks as a result of decrease in the crystallite size of both Al and CuO.

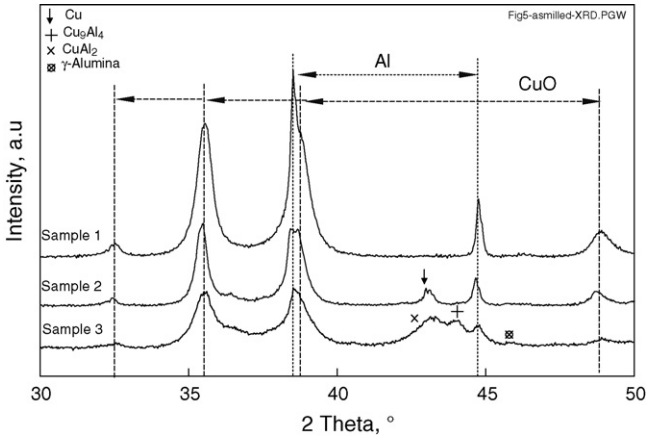

Fig. 5. X-ray diffraction patterns of composite samples 1–3.

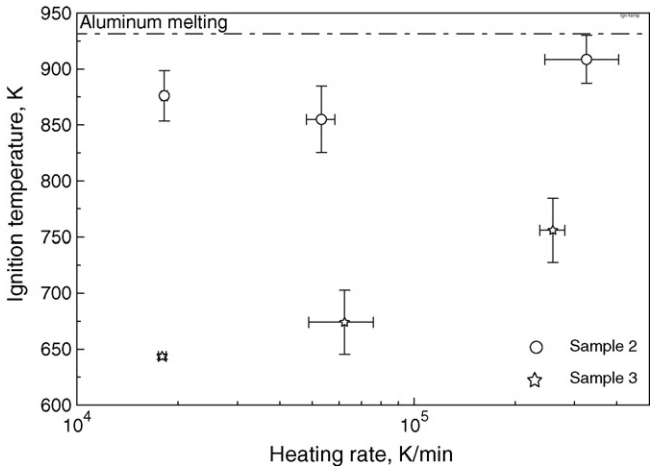

Fig. 6. Ignition temperatures measured for samples 2 and 3 at different heating rates. The error bars represent the standard deviations from multiple measurements.

SEM and XRD results indicated that sample 1 consisted of unmixed particles of the starting material. Hence the ignition experiments and thermal analysis measurements were limited to samples 2 and 3 in which nanocomposite structures were formed.

3.3. Ignition

Fig. 6 shows the ignition temperatures of the Al–CuO nanocomposites as a function of heating rate. The filament ignition experiments were performed in air at three different heating rates varying in the range of 10^4 to 10^6 K/min (10^3 to 10^4 K/s). In general it is observed that the ignition temperatures of the Al–CuO nanocomposites increase with increasing heating rates as is expected for a thermally activated ignition mechanism. It is also clear that ignition temperatures measured for sample 2 are higher than for sample 3. A decrease in the ignition temperature for sample 3 can be attributed to a higher degree of structural refinement achieved at a longer milling time with a greater quantity of liquid process control agent.

3.4. Thermal analysis

Thermal analysis was performed in both argon and oxygen environments for several heating rates. Fig. 7 shows the DSC traces of samples 2 and 3 collected at 5, 20 and 40 K/min in argon. The traces shown were baseline-corrected by subtracting the signal recorded during the second heating of the same sample. Heating of sample 2 from room temperature to 1013 K was accompanied by a broad and very weak exothermic event between 350 and 800 K. In addition, a strong exothermic peak was observed between 825 and 930 K. A weak endothermic peak corresponding to aluminum melting was observed around 933 K.

The DSC trace of sample 3 is characterized by a series of at least 3 overlapping exothermic events, including the low temperature events that were not observed for sample 2. The first, broad exothermic event was observed between 350 and 600 K. It was followed by a strong exothermic event between 600 and 800 K.

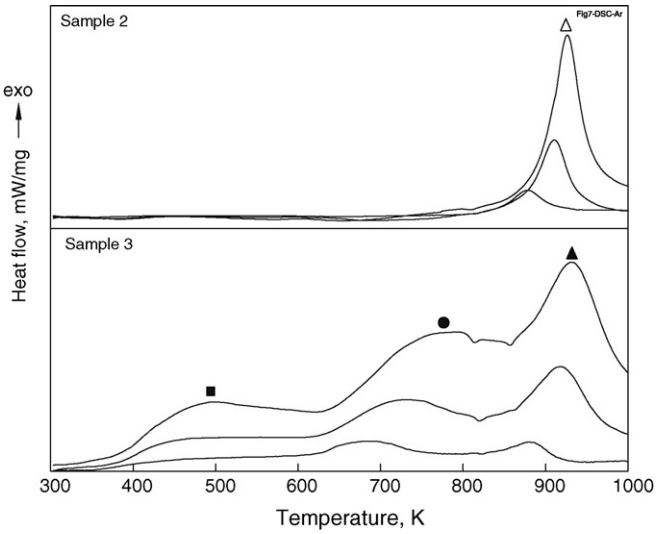

Fig. 7. DSC traces of samples 2 and 3, recorded in argon at the heating rates of 5, 20 and 40 K/min, respectively. Symbols are used to identify the exothermic peaks.

The third exothermic event occurred between 825 and 930 K and was similar to the exothermic peak observed for sample 2 in the same temperature range. In addition to the aluminum-melting peak, endothermic peaks were observed around 820 and 860 K, corresponding to the melting of $CuAl_2$ and Cu_9Al_4, respectively [18].

To identify processes occurring during the exothermic events, XRD patterns were collected from powders obtained by quenching sample 3 heated to intermediate temperatures bracketing each event. The sample was quenched by interrupting the power to the DSC furnace, achieving effective cooling of 300–500 K over a period of 10–15 min. Fig. 8 shows the respective XRD patterns.

The XRD pattern of the as-milled material is shown in Fig. 8 for reference as well and is identical to that shown in Fig. 5 for sample 3. As a general trend, the peak intensities for starting materials Al and CuO, decrease, whereas the peak intensities of the reaction products, e.g., Cu_2O, $CuAl_2$, Cu_9Al_4 and γ-Al_2O_3

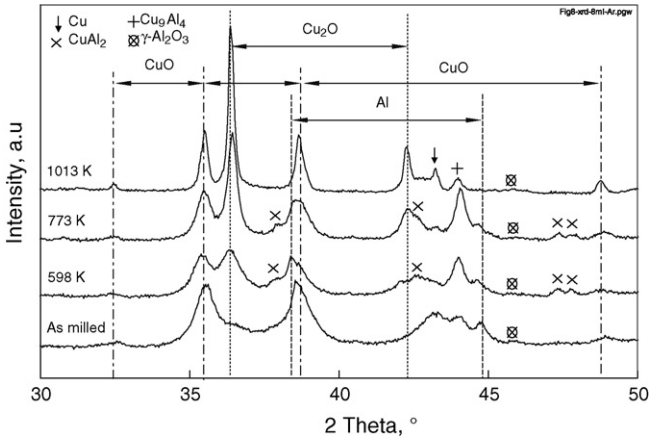

Fig. 8. XRD patterns of the powders produced by heating sample 3 in argon to and quenching at the temperatures bracketing exothermic events observed in DSC traces (Fig. 7).

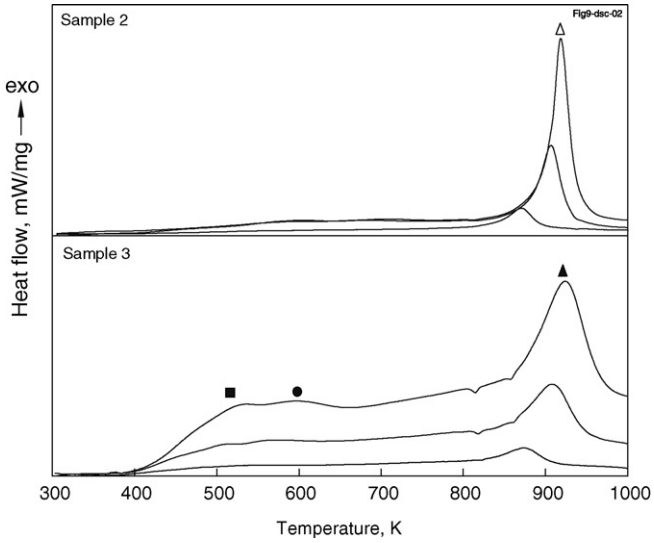

Fig. 9. DSC traces of samples 2 and 3, recorded in oxygen at the heating rates of 5, 20 and 40 K/min, respectively. Symbols are used to identify the exothermic peaks.

increase at higher temperatures. The main effect observed for the sample heated to 598 K, is a substantial increase in intensity of the Cu_2O peaks. This increase continues throughout the heating. The peaks of intermetallic phases, $CuAl_2$, Cu_9Al_4 become fairly strong at 598 and 773 K, but almost disappear at a higher temperature. The intensity of peaks corresponding to both Cu_2O and Cu increases considerably at 1013 K. It was also observed that the peaks become narrow as the temperature increases, which implies that crystallite sizes of the materials increase.

Fig. 9 shows the DSC traces of samples 2 and 3 heated at 5, 20 and 40 K/min in oxygen. The traces shown were baseline-corrected by subtracting the signals recorded during the second heating of the same sample. DSC traces generally similar to those recorded for the same samples heated in argon, as shown in Fig. 7. However, the positions of the low-temperature exothermic events observed for sample 3 in oxygen are slightly shifted compared to those in argon.

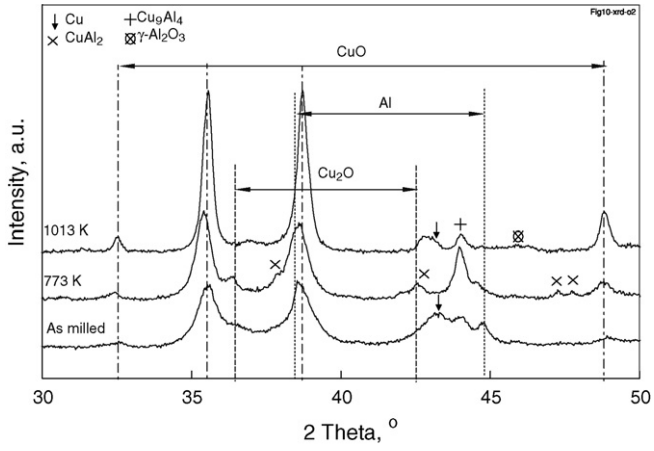

Fig. 10. XRD patterns of the powders produced by heating sample 3 in oxygen to and quenching at the temperatures bracketing exothermic events observed in DSC traces (Fig. 9).

Similar to the treatment described above for the samples heated in argon, the powders produced by heating sample 3 in oxygen and quenching at several intermediate temperatures were collected and analyzed by XRD. Fig. 10 shows the respective XRD patterns. Unlike results shown in Fig. 8, the peak intensity of CuO increases at increased temperatures, while the peak intensity of Al decreases as in Fig. 8. Only a small increase in the peak intensity for Cu_2O at 773 K is observed followed by a decrease at 1013 K. Similar to results shown in Fig. 8, the intensity of the peaks of intermetallic phases is at a maximum at the intermediate temperature of 773 K. Also similar to Fig. 8, the peak intensity of Cu increases considerably at 1013 K and all the peaks become narrow at increased temperatures indicating an increase in the crystallite sizes.

4. Reaction kinetics

The thermal analysis data were initially processed using an isoconversion method by Kissinger [19]. A plot of $\ln(\beta/T^2)$ versus the reciprocal temperatures $1/T$ of the DSC peaks, where β is the heating rate in K/min, is shown in Fig. 11. In addition, the results of the ignition temperature measurements are presented in the same coordinates, corresponding to a much higher range of heating rates. The slopes of the straight lines corresponding to each group of data points represent the values for the respective activation energies. Results of DSC experiments obtained for samples 2 and 3 in argon are shown in Fig. 11. Table 2 summarizes the activation energies obtained by the Kissinger method for the exothermic peaks observed for both samples 2 and 3 heated in both argon and oxygen environments.

Fig. 11 shows that when the heating rates approach the range of those used in ignition experiments, the stronger exothermic events (labeled as (▲) and (●) in Figs. 7 and 11) are expected to occur at much higher temperatures, as compared to the observed ignition temperatures. Note that the points representing the strong peak labeled as (△), for sample 2, nearly coincide with the points representing the strong peak labeled as

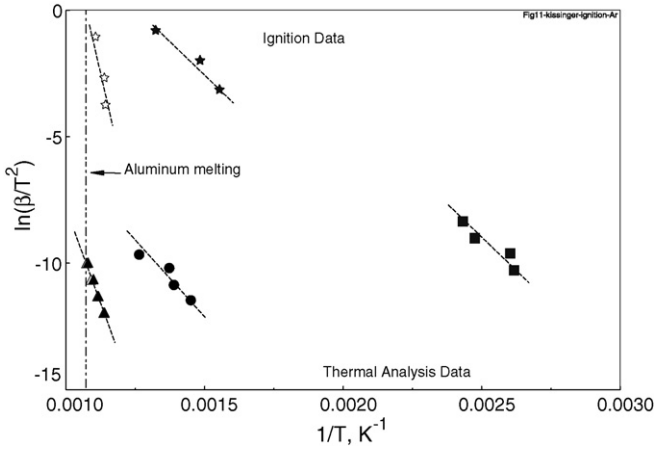

Fig. 11. Comparison of ignition temperatures measured at different heating rates in air and exothermic peak positions observed in the DSC traces for samples 2 and 3 heated in argon. The hollow and solid symbols represent data for samples 2 and 3, respectively. The aluminum melting point is shown for reference.

Table 2
Activation energies of exothermic peaks observed in argon and oxygen for sample 3 calculated using Kissinger method [19]

Sample ID	Exothermic peak description/respective symbol in Figs. 7 and 9		E_A (kJ/mol) DSC environment	
			Argon	Oxygen
Sample 2	Strong peak	△	277	268
Sample 3	Broad peak	■	70	119
	Strong peak	●	80	91
	Strong peak	▲	260	259

(▲) for sample 3. Note also that ignition of sample 2 occurs at temperatures that are weakly dependent on the heating rate and are very close to the melting point of Al (cf. Fig. 6). The kinetics of the low-temperature, relatively weak and broad exothermic event labeled as (■), seems to project to a temperature range close to, but slightly lower than that observed for ignition of sample 3 (cf. Fig. 11).

The following discussion will be only related to sample 3, for which ignition occurred at lower temperatures and appeared to be most directly affected by low-temperature Al–CuO reactions of interest in this paper. Because of the higher level of refinement (cf. Figs. 3–5), sample 3 best represented nanocomposite Al–CuO materials of interest to practical applications.

A useful correlation between the thermal analysis results and ignition experiments can only be established if the reaction kinetics representing the exothermic events observed in DSC are described quantitatively. As a first step to obtaining such a description, the DSC traces for sample 3 were processed to determine the activation energy as a function of reaction progress, α, according to the method after Ozawa [20], and Flynn and Wall [21]. This processing was based on evaluation of temperatures corresponding to a constant reaction progress observed at different heating rates. Calculations of the reaction progress involved measurements of partial areas under the DSC curves, which required detailed reconstruction of the temperature-dependent baselines. Because the temperature ranges used in the experiments were broad, the baselines were neither well-constrained, nor expected to be linear. This was confirmed by initial estimates using straight-line baselines between start and end points of the DSC signal, which resulted in substantially different reaction progress corresponding to the positions of the same exothermic peaks at different heating rates. To reconstruct a more accurate temperature dependent baseline, it was assumed that the degree of conversion was the same for all heating rates when the third, strongest peak occurred in the DSC signals. The initial and final slopes of the DSC curve recorded at 5 K/min were used to construct a smooth initial baseline for this measurement and determine the respective degree of conversion corresponding to the position of the 3rd peak. This degree of conversion corresponded to 90%, and it was used consistently to adjust the baseline representing the weighted averages of the initial and final slopes for other used heating rates.

Using the reconstructed baselines, the activation energy was calculated as a function of reaction progress as shown in Fig. 12. The temperatures corresponding to the reaction progress of 20, 40, 60, and 90% for the heating rate of 5 K/min are also shown in Fig. 12 for reference.

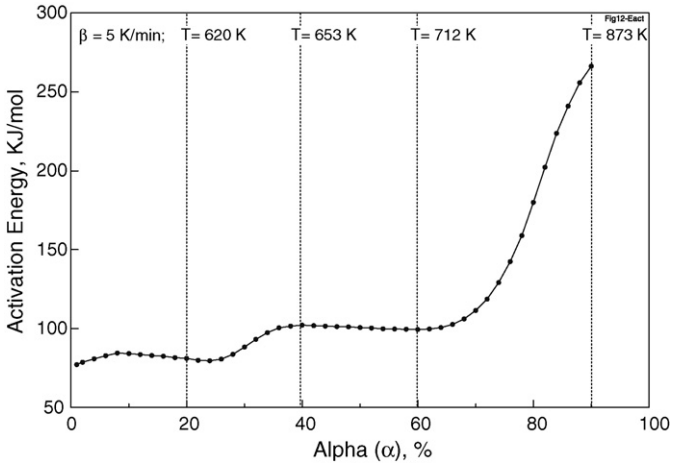

Fig. 12. Activation energy as a function of reaction progress, α. The dotted lines indicate the reaction temperatures corresponding to the respective values of α at the heating rate of 5 K/min.

The initial value of the activation energy remains close to 80 kJ/mol until a reaction progress of about 30%. This is followed by a segment with an activation energy close to 100 kJ/mol. After about 70% of the overall reaction is completed, the activation energy increases to about 265 kJ/mol. The dependency of activation energy on the reaction progress indicates that at least three different reaction steps need to be considered. This is consistent with the overall DSC signal shape indicating at least three overlapping exothermic events as discussed above. The values of activation energies are also roughly consistent with those shown in Table 2, found from the peak position processing using the Kissinger method. Following this initial assessment, the reaction was assumed to comprise three separate steps with the respective activation energies defined from the flat portions of the curve shown in Fig. 12. This initial assumption was explored using Netzsch Thermokinetics software [22]. A sequence of calculations was performed in which the activation energies of the three steps remained fixed but the reaction mechanisms and frequency factors were allowed to change to match the experimental results at different heating rates. In addition, the reaction scheme was varied starting with three independent parallel reactions and including different combinations of interdependent reactions occurring in series or in parallel. After a number of calculations, it was found that a close match of the shape of the low-temperature portion of the DSC trace could not be achieved. Thus, it was further assumed that the broad, low-temperature exothermic event corresponding to α up to about 30% consists of two overlapping reaction steps with close activation energies, but different frequency factors and, possibly, reaction mechanisms. A second set of calculations with four reaction steps was therefore performed in which, as described earlier, various combinations of reaction mechanisms and reaction models were considered. As before, the activation energies remained restricted in the three narrow ranges, as implied by the three levels observed in Fig. 12. While

Table 3
Kinetic parameters for the reaction steps used to describe DSC traces for sample 3

No.	Approximate temperature range (K)	Reaction type	Kinetic expression $f(\alpha)$	n	E_a (kJ/mol)	log(A) (s^{-1})
1	350–550	Avrami–Erofeev n-dimensional nuclear/growth	$n(\alpha-1)\ln(1-\alpha)^{(n-1)/n}$	0.6	78	6.68
2	450–650	nth order	$(1-\alpha)^n$	3.9	79	5.15
3	600–800	nth order	$(1-\alpha)^{(n}$	2.6	102	5.03
4	850–1000	Avrami–Erofeev n-dimensional nuclear/growth	$n(\alpha-1)\ln(1-\alpha)^{(n-1)/n}$	0.75	266	13.3

the results were quite sensitive to the selection of individual reaction mechanisms and frequency factors, no significant improvement could be achieved assuming complex interdependent reaction schemes as opposed to the simplest assumption of four independent, parallel reactions. Thus, it was finally found that a reaction mechanism including four independent parallel reactions as described in Table 3 provides an adequate match of the experimental DSC traces at different heating rates. The first, low temperature step was modeled as an Avrami–Erofeev n-dimensional nucleation/growth controlled reaction [23] with $n = 0.6$. The second and third steps were modeled as n^{th} order reactions with $n = 3.9$ and 2.6, respectively. The fourth step was modeled with an Avrami–Erofeev n-dimensional nucleation/growth controlled reaction with $n = 0.75$.

Fig. 13 shows a comparison of experimental and calculated DSC traces for different heating rates. Curves illustrating individual reaction steps, as described in Table 3 are also shown. In addition, the predicted DSC signal, or the calculated rates of heat release are presented for the higher heating rates approaching those realized in the ignition experiments. Because of different activation energies, the shapes of the traces change and it becomes increasingly difficult to distinguish between contributions from individual reaction steps.

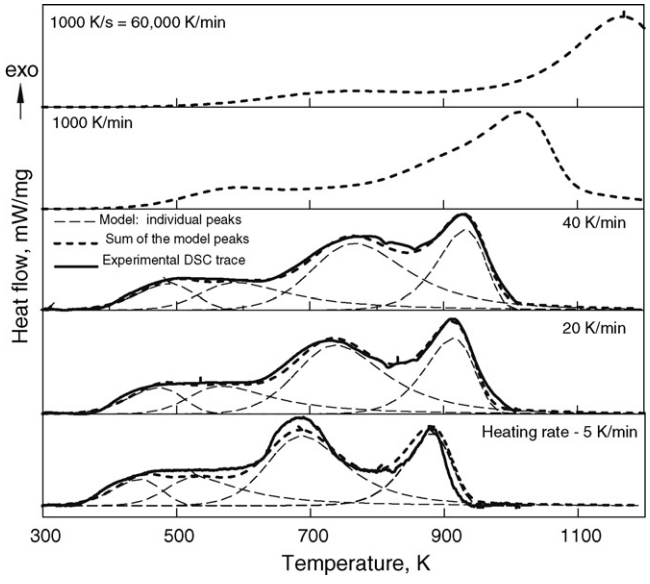

Fig. 13. Comparison of experimental (solid lines) and calculated DSC traces (dashed lines) for different heating rates. Thin dashed lines show individual reaction steps. Predicted heat flows are also shown for high heating rates approaching the experimental conditions for ignition tests.

5. Discussion

The experimental DSC data for different samples were observed to be somewhat different. The results for sample 2, for which the level of structural refinement was relatively low, were similar to the earlier results [6,7] presented for multilayer Al–CuO_x nanofoils. The first well resolved exothermic peak occurred in the vicinity of 900 K. The activation energy for this peak was estimated to be around 270 kJ/mol (Table 2), which compares well with the value of about 280 kJ/mol reported in ref. [7]. The low-temperature processes resulted in a small, low-temperature exotherm that was clearly detected but poorly resolved for sample 2. On the other hand, these low-temperature events were well resolved for sample 3, which had the same chemical composition as sample 2, but was prepared with a better refinement and a more uniform nanomixing between Al and CuO. Thus, the analysis of the reaction kinetics presented above for sample 3 describes the generic thermite reaction 2Al + 3CuO, with a higher reaction rate due to the very high reactive interface area. In terms of thermally activated reaction models, the description obtained by processing specific DSC signals for sample 3 will have values of pre-exponents (or frequency factors) specific for that sample, while the rest of the model should be applicable to any Al–CuO thermites. The quantitative correlation of the frequency factors with the specific sample morphology was beyond the scope of this project but is planned in the future.

The differences observed between the DSC signals recorded for both samples 2 and 3 in oxygen and argon are insignificant. The analysis of intermediate reaction products shows that the reactions in argon start from decomposition of CuO to Cu_2O. The bulk of the released oxygen must have oxidized aluminum in order to explain the observed significant exothermic effect. Thus, it is suggested that amorphous or poorly crystalline aluminum oxide polymorphs were produced even though they were not well visible from the XRD patterns.

For both samples, the initial exothermic effect was nearly the same in oxygen, as it was in argon while the formation of Cu_2O was not detected from XRD for the samples heated in oxygen. This can be interpreted suggesting that the produced Cu_2O quickly re-oxidized interacting with the ambient oxygen. This difference in the reaction products explains the small differences in the reaction kinetics (cf. Table 2). Thus, the reaction kinetics measured for experiments in oxygen represents an additional process of re-oxidation of the produced Cu_2O that is unlikely for the rapid processes occurring in practical applications and in the performed here ignition experiments. Therefore, the

heterogeneous reaction kinetics applicable for use in ignition models needs only to describe the reactions in the Al–CuO system, without adding reactions with external oxygen. Such a kinetic model was developed above (cf. Table 3) considering the DSC results produced by heating sample 3 in argon.

The proposed model involving four independent parallel reaction steps describes consistently the experimental thermal analysis data. It is interesting to consider which specific reactions could be tentatively assigned to the four steps that were introduced. The comparison can be now made between the kinetic parameters identified in Table 3 and those reported in the literature for related reactions in the Al–CuO systems.

Relatively low activation energies were reported for the processes involving decomposition of CuO. The activation energy of reduction of CuO in the presence of hydrogen was found to be 60 kJ/mol [24]. In another report, the reaction $4CuO \rightarrow 2Cu_2O + O_2$ taking place via a moving phase boundary and rate limited by oxygen diffusion along the Cu_2O grain boundaries, was found to have an activation energy of 106 kJ/mol [25]. On the other hand, activation energies in a broad range have been reported for the aluminum oxidation that is rate-limited by diffusion through growing Al_2O_3 scales. A sequence of Al_2O_3 polymorphs including amorphous $\rightarrow \gamma \rightarrow \theta \rightarrow \alpha$ phases was reported to be produced upon aluminum heating in oxygenated gases [26]. This sequence is expected to be modified by the presence of other condensed phases, such as CuO_x, but the overall scheme of aluminum oxidation including a sequence of transition alumina phases leading to the formation of the stable α-Al_2O_3 should remain. The related activation energies for the consequent oxidation steps of aluminum powders in oxygen were identified in ref. [27] as 120, 227, and 306 kJ/mol for the growth of amorphous, γ- and α-alumina polymorphs, respectively.

Interestingly, the initial process of growth of the amorphous alumina has the activation energy comparable to that of CuO decomposition. However, the activation energy increases significantly upon formation of crystalline alumina polymorphs at higher temperatures.

Comparing the activation energies reported in the literature for CuO decomposition and alumina growth with the values presented in Table 3, it can be suggested that the initial steps of the Al–CuO reaction are controlled by CuO decomposition. This suggestion is supported by the XRD patterns analyzed for the samples quenched from intermediate temperatures. At higher temperatures, the rates of these decomposition processes are supplemented by the growth of amorphous alumina that could not be detected by XRD. The above processes can be assigned for the introduced steps 1–3 which all have relatively low activation energies. An increase in the activation energy in step 4 signals that the growth of crystalline Al_2O_3 polymorphs becomes the rate-limiting reaction step.

Because the four events were assumed to be independent of one another, the total heat release of thermite reaction can be found simply as a sum of the heats released in each event

$$\dot{Q}_{\text{total}} = \sum_{i=1}^{4} \dot{Q}_i \quad (1)$$

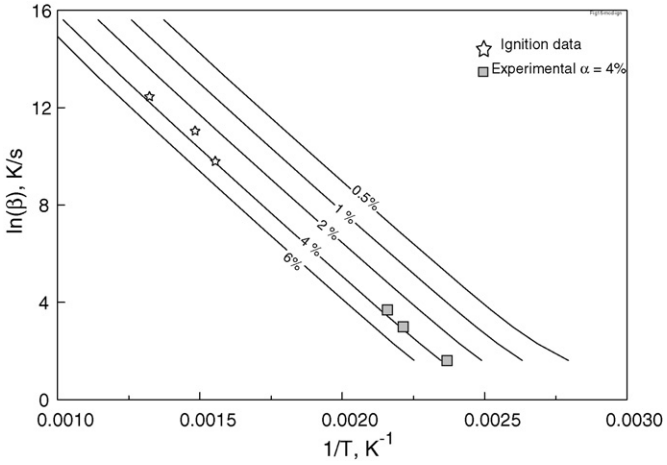

Fig. 14. Comparison of ignition experiments and thermal analysis data at selected levels of reaction progress with the lines of constant reaction progress calculated according to the introduced kinetic model.

Considering specific expressions and parameters of individual terms, $\dot{Q}_i$, described in Table 3, the heat release as a function of temperature and heating rate for the overall Al–CuO thermite reaction can now be described. As noted above, the frequency factors are specific for the particular sample morphology used in this research and one needs to re-determine their values for different nanocomposite materials. The overall reaction mechanism, however, is expected to remain valid for any Al–CuO composites.

In order to use the proposed reaction mechanism for quantitative description of ignition experiments, a detailed heat transfer model needs to be developed describing the ignition experiment and including the term given by Eq. (1), using the specific kinetic parameters presented in Table 3. Such a model was outside the scope of this project. Instead, the validity of the proposed mechanism was assessed by relating thermal analysis to ignition experiments via an isoconversion approach. This assumes that ignition occurs at a constant degree of reaction progress α (see Fig. 12). Fig. 14 shows an Arrhenius diagram where a group of curves representing constant reaction progress are superimposed on the experimentally observed ignition temperatures. The plot suggests that ignition occurs when approximately 4% of the total reaction enthalpy is released. The temperatures where 4% reaction progress is observed in the thermal analysis experiments have been determined and are also shown for reference. These experimental points correlate well with the calculated lines of constant reaction progress, which is to be expected considering the good match between the experimental and calculated DSC curves shown in Fig. 13. This indicates that ignition indeed can be described adequately by the overall reaction kinetics model reported here.

6. Conclusions

The highly exothermic heterogeneous reaction between Al and CuO was found to start at relatively low temperatures (~400 K) and is well described by four parallel reaction steps. Earlier measurements did not resolve the low-temperature

exothermic events and focused on the strongest, fourth reaction step. However, ignition of the nanocomposite Al–CuO materials was shown to be driven primarily by the lower-temperature oxidation processes.

Specific mechanisms and kinetic parameters were determined to describe the individual reaction steps for the prepared nanocomposite powders. These mechanisms include the frequency factors specific for the powders used in this study and activation energies that should remain valid for any Al–CuO composite materials. The identified reaction steps were tentatively assigned to specific processes of CuO decomposition followed by diffusion of reacting species through amorphous and then crystalline Al_2O_3 polymorphs. It was shown that ignition of Al–CuO nanocomposite powders can be described reasonably well using the proposed kinetics of Al–CuO heterogeneous reactions. Future work will focus on development of a complete, quantitative ignition model.

Acknowledgements

This work was supported in parts by Defense Threat Reduction Agency, Award DAAE30-01-9-0080 (Dr. William Wilson) and Office of Naval Research, Grant N00014-00-1-0446 (Dr. Judah Goldwasser).

References

[1] S.F. Son, B.W. Asay, J.R. Busse, B.S. Jorgensen, B. Bockmon, M. Pantoya, Proceedings of the International Pyrotechnic, The Twenty-eighth International Pyrotechnics Seminar, Adelaide, Australia, November 4–9, 2001.
[2] D.S. Moore, S.F. Son, B.W. Asay, Propellants Explos. Pyrotech. 29 (2) (2004) 106–111.
[3] J.J. Granier, M.L. Pantoya, Combust. Flame 138 (2004) 373–383.
[4] A.E. Gash, T.M. Tillotson, J.H. Satcher, L.W. Hrubesh Jr., R.L. Simpson, J. Non-Cryst. Solids 285 (2001) 22–28.
[5] T.M. Tillotson, A.E. Gash, R.L. Simpson, L.W. Hrubesh Jr., J.H. Satcher, J.F. Poco, J. Non-Cryst. Solids 285 (2001) 338–345.
[6] K.J. Blobaum, M.E. Reiss, J.M. Plitzko Lawrence, T.P. Weihs, J. Appl. Phys. 94 (5) (2003) 2915–2922.
[7] K.J. Blobaum, A.J. Wagner, J.M. Plitzko, D. Van Heerden, D.H. Fairbrother, T.P. Weihs, J. Appl. Phys. 94 (5) (2003) 2923–2928.
[8] M. Schoenitz, T. Ward, E.L. Dreizin, Mater. Res. Soc. Symp. Proc. 800 (2004) AA2.6.1–AA2.6.6.
[9] E.L. Dreizin, M. Schoenitz, Nano-Composite Energetic Powders Prepared by Arrested Reactive Milling, US Patent Application 20060053970, published in March, 2006.
[10] M. Schoenitz, T.S. Ward, E.L. Dreizin, Proc. Combust. Inst. 30 (2005) 2071–2078.
[11] L. Takacs, Prog. Mater. Sci. 47 (2002) 355–414.
[12] P. Balaz, L. Takacs, E. Boldizarova, E. Godocokova, J. Phys. Chem. Solids 64 (2003) 1413–1417.
[13] S. Umbrajkar, X. Zhu, M. Schoenitz, E. Dreizin, Proceedings of the Fourth Joint Meeting of the U.S. Sections of the Combustion Institute, Philadelphia, March 23–25, 2005, Combustion Institute, Pittsburg, PA, 2005.
[14] Y.L. Shoshin, M.A. Trunov, M. Schoenitz, X. Zhu, E.L. Dreizin, Combust. Flame 144 (2006) 688–697.
[15] M.A. Trunov, M. Schoenitz, E.L. Dreizin, Novel energetic materials and application, in: L. DeLuca, L. Galfetti, R.A. Pesce-Rodriguez (Eds.), Edited Book of Proceedings of the Ninth International Workshop on Combustion and Propulsion Arzago d'Adda, BG, Italy, 2004, pp. 9.1–9.13.
[16] T.S. Ward, M.A. Trunov, E.L. Dreizin, Proceedings of the Fourth Joint Meeting of the U.S. Sections of the Combustion Institute, Philadelphia, March 23–25, 2005, Combustion Institute, Pittsburg, PA, 2005.
[17] Table of emissivity of various surfaces by Micron Instrument Company, Inc., http://www.transmetra.ch/pdf/publikationen/emissivity.pdf.
[18] A. Butts, Copper: The Science and Technology of the Metal its Alloys and Compounds, Hafner Publishing Company, Inc., 1970, pp. 460–462.
[19] H.E. Kissinger, Anal. Chem. V 29 (1957) 1702–1706.
[20] T. Ozawa, Bull. Chem. Soc. Jpn. 38 (1965) 1881–1886.
[21] J.H. Flynn, L.A. Wall, J. Res. Natl. Bur. Stand. Sect. A 70 (1966) 487–523.
[22] J. Opfermann, NETZSCH Thermokinetics 2, Version 04, NETZSCH Gerätebau GmbH, 2005.
[23] J. Opfermann, J. Thermal Anal. Calorimetry 60 (2) (2000) 641–658.
[24] J.Y. Kim, J.A. Rodriguez, J.C. Hanson, A.I. Frankel, P.L. Lee, J. Am. Chem. Soc. 125 (2003) 10684–10692.
[25] J. Li, S.Q. Wang, J.W. Mayer, K.N. Tu, Phys. Rev. B 39 (16) (1989) 12367–12372.
[26] I. Levin, D. Brandon, J. Am. Ceram. Soc. 81 (1998) 1995–2012.
[27] M.A. Trunov, M. Schoenitz, X. Zhu, E.L. Dreizin, Combust. Flame 140 (4) (2005) 310–318.